Tunable Angle-Dependent Magnetization Dynamics in $Ni_{80}Fe_{20}$ Nanocross Structures of Varying Size

Kartik Adhikari,[1] Saswati Barman,[2] Ruma Mandal,[1] Yoshichika Otani,[3,4] and Anjan Barman[1,*]

[1] *Department of Condensed Matter Physics and Material Sciences, S. N. Bose National Centre for Basic Sciences, Block JD, Sector III, Salt Lake, Kolkata 700106, India*

[2] *Institute of Engineering and Management, Sector V, Salt Lake, Kolkata 700091, India*

[3] *CEMS-RIKEN, 2-1 Hirosawa, Wako, Saitama 351-0198, Japan*

[4] *Institute for Solid State Physics, University of Tokyo, 5-1-5 Kashiwanoha, Kashiwa, Chiba 277-8581, Japan*

(Received 4 June 2018; revised manuscript received 8 September 2018; published 3 October 2018)

We demonstrate a large angular dependence of magnetization dynamics in $Ni_{80}Fe_{20}$ nanocross arrays of varying sizes. By subtle variation of the azimuthal angle (ϕ) of an in-plane bias magnetic field, the spin configuration and the ensuing spin-wave dynamics, including mode softening, mode splitting, mode crossover, and mode merging, can be drastically varied to the extent that a frequency minimum corresponding to mode softening converts to a mode crossover, various mode splitting and mode crossover disappear, and additional mode splitting appears. Numerically simulated spin-wave spectra and phase profiles reveal the nature of various spin-wave modes and the origin of the above variation of the dynamics with a bias-field angle. All of these above observations are further modified with the variation of the dimensions of the nanocross. The numerically calculated magnetostatic field distributions further support the variation of dynamics with a bias-field angle. These results open an avenue for engineering nanocross-based magnetic devices such as magnetic storage, spin-wave logic, and on-chip data communication devices.

DOI: 10.1103/PhysRevApplied.10.044010

I. INTRODUCTION

Arrays of nanoscale ferromagnetic dots [1] have attracted wide interest in recent years, both in terms of fundamental physics as well as for their potential applications. During the last decade, investigation of spin dynamics and spin wave (SW) [2] in such nanostructures has emerged as a very potent research area. This interest is triggered by the possibility of exploring new physics in such structures. On the other hand, due to the progress of nanolithography [3], patterned nanostructures and their arrays have emerged as systems having great potential applications such as magnetic data storage [4,5], memory [6], logic devices [7], and spin-torque nano-oscillators [8]. In nanodot arrays [9], the high surface-to-volume ratio, inhomogeneous demagnetizing field, dipole-dipole [10,11] interaction between the nanodots have significant effects on their magnetic properties and can lead to complex spin configurations within a single nanomagnet [12,13] and arrays of nanomagnets [14–20]. These complex spin configurations lead to rich variety of SW modes which have strong dependence on the strength [15] and orientation [16,17] of the applied bias magnetic field, and on the shape [18–20] and size [9,32] of nano-elements. Extensive research work has been carried out to experimentally investigate the magnetization dynamics in two-dimensional (2D) arrays of nanomagnets using time-resolved scanning Kerr microscopy (TRSKM) [21] or time-resolved magneto-optical Kerr effect (TRMOKE) microscopy [22], ferromagnetic resonance (FMR) [23–25], and Brillouin light scattering (BLS) [26,27]; and theoretically by micromagnetic simulations [28] and other numerical and analytical methods. While the optical techniques can extract information about the local behavior of the dynamics, the ferromagnetic resonance can measure the global dynamics of a large array. In addition, due to its advantage of being a much faster measurement technique, very detailed investigations of bias-field strength and angle-dependence study can be made using this technique.

Ferromagnetic cross structure has received some interest in the magnetism community due to its complex spin configuration [29]. However, the ultrafast magnetization dynamics measured by the TRMOKE has revealed very rich dynamics with a strong configurational anisotropy [30]. Later in 2015, a report [31] proposed that ferromagnetic cross-shaped elements can be used as reconfigurable spin-based logic devices using SW scattering and interference. A more recent study [32] on cross-shaped nanodot

*abarman@bose.res.in

arrays using broadband FMR measurements showed a bias-field-tunable magnetic configuration and magnetization dynamics, including the presence of mode softening and mode crossover. The above results have opened up the possibility of applications of ferromagnetic nanocross structures as a potential building block for magnetic storage, memory, on-chip data communication, and spin-based logic devices, and hence, thorough investigation of the magnetization dynamics of this structure with its geometric parameters and external magnetic fields has become imperative. Here, we present the experimental and numerical study of the tunability of magnetization dynamics in $Ni_{80}Fe_{20}$ (permalloy, Py hereafter) nanocrosses of varying arm lengths (L) with in-plane orientation of the bias magnetic field. We use broadband FMR technique and micromagnetic simulations for this work. We show that SW mode softening can be efficiently tuned by a subtle variation of the bias magnetic field orientation. Further properties such as SW mode splitting, mode crossover, mode merging, and the number of modes can also be easily tuned by bias-field orientation, which significantly depend on the size of the nanocross element. We finally discuss some possible applications of the nanocross arrays based on our observations.

II. EXPERIMENTAL DETAILS

Arrays (200×20 μm^2) of Py nanocrosses with arm length (L) varying between 400 nm $\leq L \leq$ 600 nm, and constant edge-to-edge separation (S) of 150 nm and thickness of 20 nm, as well as a continuous Py film of 20-nm thickness were fabricated on a self-oxidized Si substrate (001) by a combination of e-beam lithography and e-beam evaporation. Py film of 20-nm thickness coated with a 60-nm-thick Al_2O_3 protective layer was deposited in an ultra-high vacuum chamber at a base pressure of 2×10^{-8} Torr on a bilayer polymethyl methacrylate/methyl methacrylate (PMMA/MMA) resist pattern on the Si substrate made by using e-beam lithography. A coplaner waveguide (CPW) made by Au of 150-nm thickness, 30-μm central conductor width, 300-μm length, and 50-Ω nominal characteristic impedance is deposited on top of the nanocross structures and the continuous Py film at a base pressure of 6×10^{-7} Torr. Subsequently, a Ti protective layer of 5-nm thickness is deposited on top of the Au layer at the same base pressure. The waveguide is patterned by using maskless photolithography. The broadband FMR experiments are performed using a vector network analyzer (Agilent, PNA-L N5230C, 10 MHz to 50 GHz) and a homebuilt high-frequency probe station with a nonmagnetic G-S-G type probe (GGB Industries, Model No. 40A-GSG-150-EDP) [33]. A microwave output excitation is swept in a broad frequency range with a power of -15 dBm and fed into the CPW structure, generating a microwave magnetic field h_{rf} along the y axis of the nanocross array. Additionally, an in-plane magnetic field, H, is applied along a varying in-plane angle ϕ with respect to the x axis and the output signal (S_{11}) is collected from the CPW in the reflection geometry. The measured reflection spectra are normalized by a reference measurement at a high static magnetic field. A rotating electromagnet is used to apply an in-plane bias magnetic field up to 1.6 kOe. All the experiments are carried out at room temperature.

III. RESULTS AND DISCUSSION

Figure 1(a) shows a schematic of the experimental setup. Figures 1(b)–1(d) show scanning electron micrographs (SEMs) of all three arrays with crossarm lengths (L) of 600, 500, and 400 nm. The bias magnetic field orientation (ϕ) is shown in Fig. 1(b). The SEM images show that the cross structures suffer from some edge deformations and rounded corners, which increase with the reduction of L. The sizes of the individual crosses and their separations in the arrays also vary by up to about $\pm 10\%$. The external bias-field-(H) dependent FMR frequency (f) of the Py thin film is also measured and the data is fitted with the Kittel formula [34], which is given by

$$f = \frac{\gamma}{2\pi}\sqrt{(H + H_K)(H + H_K + 4\pi M_s)} \qquad (1)$$

to extract the magnetic parameters of the Py film. The magnetic parameters obtained from the fitting are saturation magnetization (M_s) = 850 emu/cc, gyromagnetic ratio (γ) = 17.85 MHz/Oe, and the anisotropy field (H_K) = 0. These will be further used for numerical micromagnetic

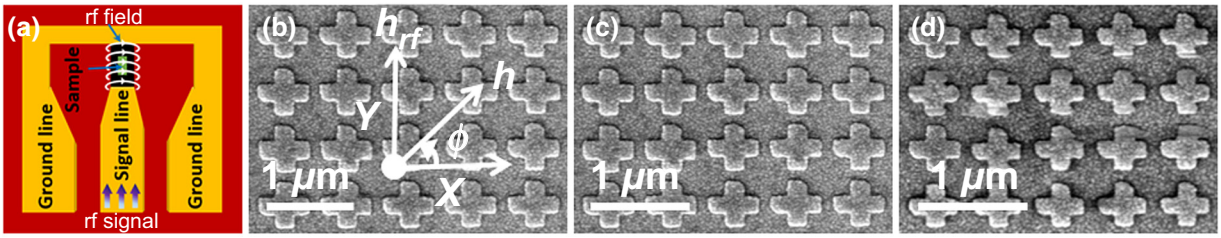

FIG. 1. (a) Schematic of our experimental geometry. (b)–(d) SEMs of $Ni_{80}Fe_{20}$ nanocross arrays with varying arm lengths. The inset shows the orientation (ϕ) of the external bias magnetic field.

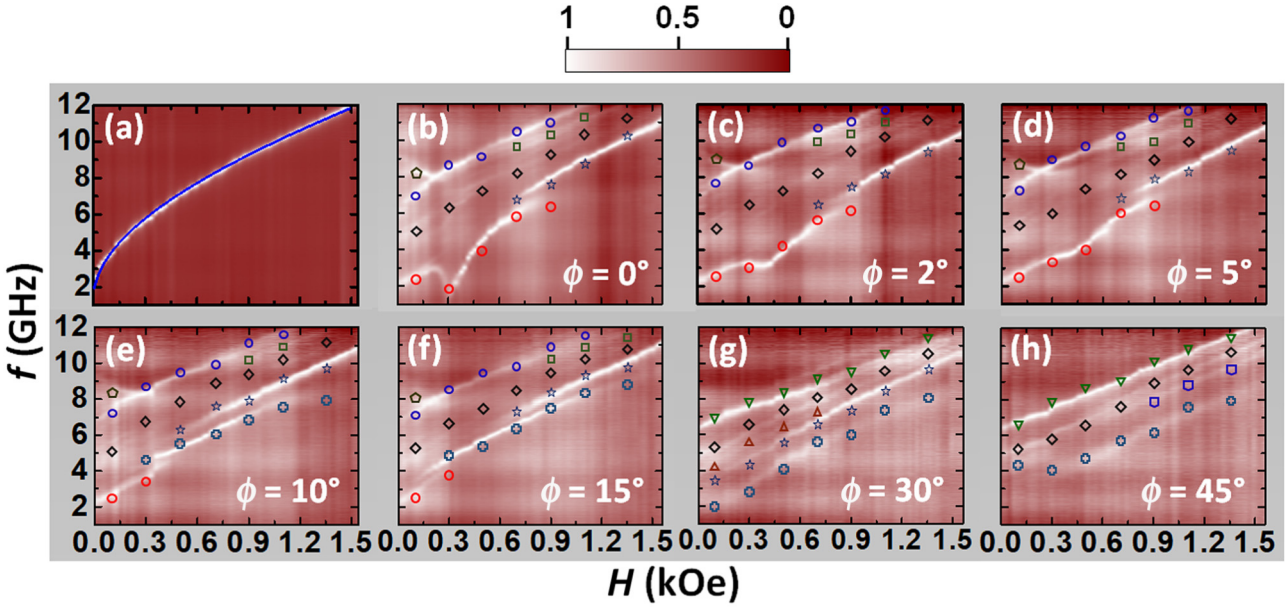

FIG. 2. Surface plots of the bias-field-dependent SW mode frequencies for (a) thin film of 20-nm thickness and nanocross array with arm length (L) of 600 nm and for the bias field orientation (ϕ) of (b) 0°, (c) 2°, (d) 5°, (e) 10°, (f) 15°, (g) 30°, and (h) 45°. (a) The Kittel fit is shown by the solid line. Simulated SW frequencies are shown by unfilled symbols. The color map is shown at the top of the figure.

simulations of the FMR spectra of the Py nanocross structures.

The bias-field-dependent FMR spectra (real part of S_{11} parameter) for Py nanocross arrays with $400\ \text{nm} \leq L \leq 600\ \text{nm}$ at different bias-field orientations are shown in Figs. 2–4. They show rich SW properties, which vary nonmonotonically with the bias-field magnitude. These include the observation of a crossover between the two lowest frequency branches, followed by sharp minima and maxima of the lowest frequency branch and merging of the two highest frequency branches followed by a Y-shaped mode splitting of the highest frequency branch with the decreasing bias field. These features are further modified by changing the nanocross dimensions, i.e., the magnitude of the bias field at which these features appear shifts toward higher field values with the reduction of the nanocross arm length. Our purpose here is to study how these fascinating features are affected by the

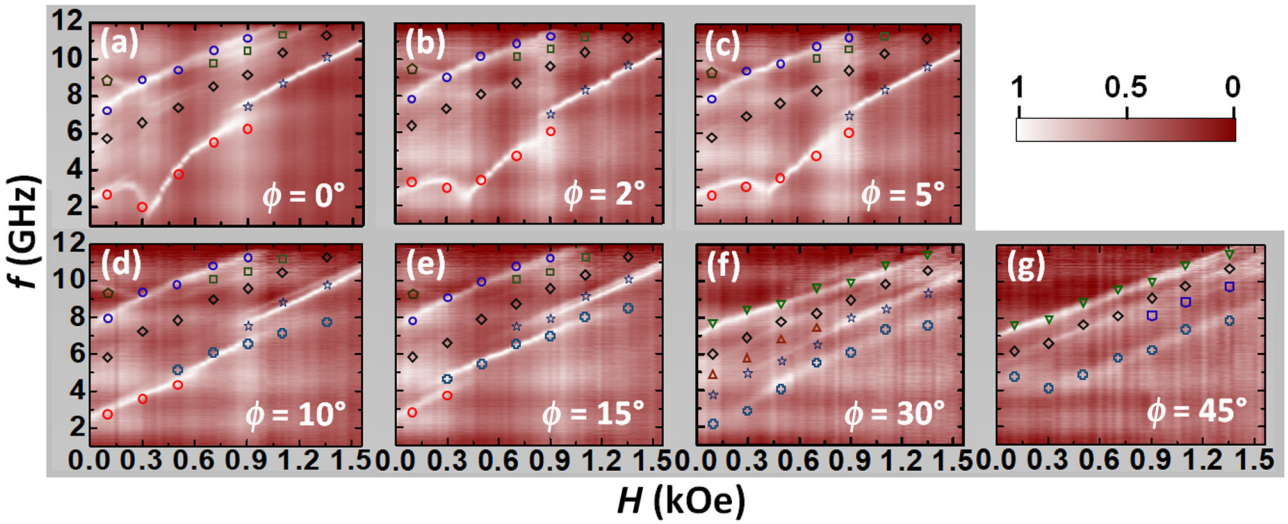

FIG. 3. Surface plots of bias-field-dependent SW mode frequencies for a nanocross array with arm length (L) of 500 nm and for the bias-field orientation (ϕ) of (a) 0°, (b) 2°, (c) 5°, (d) 10°, (e) 15°, (f) 30°, and (g) 45°. Simulated SW frequencies are shown by unfilled symbols. The color map is shown at the right side of the figure.

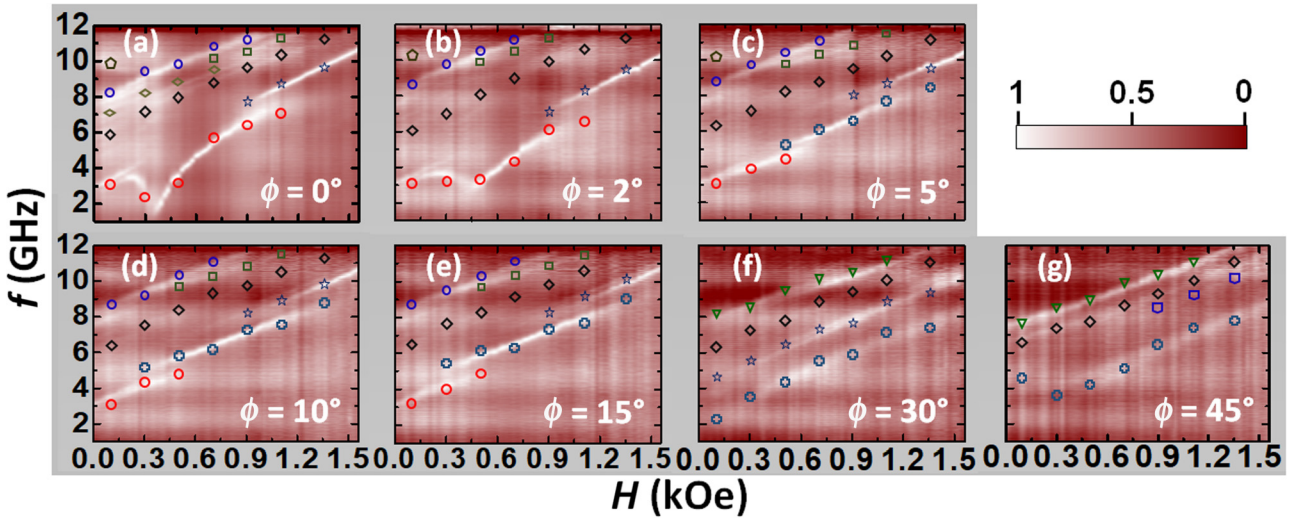

FIG. 4. Surface plots of bias-field-dependent SW mode frequencies for a nanocross array with arm length (L) of 400 nm and for the bias-field orientation (ϕ) of (a) 0°, (b) 2°, (c) 5°, (d) 10°, (e) 15°, (f) 30°, and (g) 45°. Simulated SW frequencies are shown by unfilled symbols. The color map is shown at the right side of the figure.

orientation of the bias magnetic field and whether new features can be generated.

The dip in the lowest frequency branch [Fig. 2(b)], which is a signature of mode softening appearing due to the variation in static magnetic configuration from an S state to the onion state, reduces significantly and shifts drastically to a higher field value as the bias field angle ϕ is rotated by only 2° [Fig. 2(c)]. This trend continues up to 5° [Fig. 2(d)], beyond which the dip disappears and instead a mode crossover appears at around 300 Oe for $\phi = 10°$ for the nanocross array with $L = 600$ nm. This continues up to 15°, beyond which the crossover also disappears and at $\phi = 45°$ a dip starts to appear again. The bias field for crossover between the two lowest branches at around 700 Oe suddenly extends over a broad field range at $\phi = 10°$ with the appearance of a new SW branch and the crossover completely disappears at $\phi = 30°$. The merging of the two highest frequency branches at around 500 Oe gets blurred at $\phi = 10°$ and disappears at $\phi = 30°$. The Y-shaped mode splitting of the two highest frequency branches with positive and negative slopes appearing at around 150 Oe for $\phi = 0°$ shifts to higher bias-field values with increasing values of ϕ, which finally disappears at $\phi = 30°$. With the variation of the nanocross dimensions, some more changes are observed. For example, (a) the disappearance of the dip and consequent onset of crossover for the sample with $L = 500$ nm still occurs at $\phi_a = 10°$, but the effect is rather feeble, while for $L = 400$ nm, the same occurs at $\phi_a = 5°$. (b) The disappearance of the Y-shaped mode splitting occurs at $\phi_b \approx 15°$ for $L = 600$ nm and gradually decreases to $\phi_b \approx 10°$ for $L = 500$ nm and $\phi_b \approx 5°$ for $L = 400$ nm. (c) The disappearance of mode crossover at the higher field value, on the other hand, increases from $\phi_c \approx 10°$ at $L = 600$ nm to 15° and 30° for $L = 500$ and 400 nm, respectively. (d) On the contrary, the angle for the appearance of mode splitting at a higher field value for the intermediate frequency branch remains unaltered with the arm length of the nanocross. These observations are tabulated in Table I. Here, ϕ_a, ϕ_b, ϕ_c, and ϕ_d correspond to the angles where features described as (a), (b), (c), and (d) above occur, respectively.

To interpret the experimental results, we perform micromagnetic simulations by using OOMMF [35] software. The arrays for performing the simulation are mimicked from

TABLE I. Effect of varying the dimensions of a nanocross structure on the critical angles of four prime features observed in the spin-wave dynamics.

Arm length (L)	Disappearance of mode softening and creation of new mode crossover	Disappearance of Y-shaped mode splitting at lower H value	Disappearance of mode crossover at higher H value	Appearance of mode splitting at higher H value for intermediate frequency branch
600 nm	$\phi_a \approx 10°$	$\phi_b \approx 15°$	$\phi_c \approx 10°$	$\phi_d \approx 45°$
500 nm	$\phi_a \approx 10°$	$\phi_b \approx 10°$	$\phi_c \approx 15°$	$\phi_d \approx 45°$
400 nm	$\phi_a \approx 5°$	$\phi_b \approx 5°$	$\phi_c \approx 30°$	$\phi_d \approx 45°$

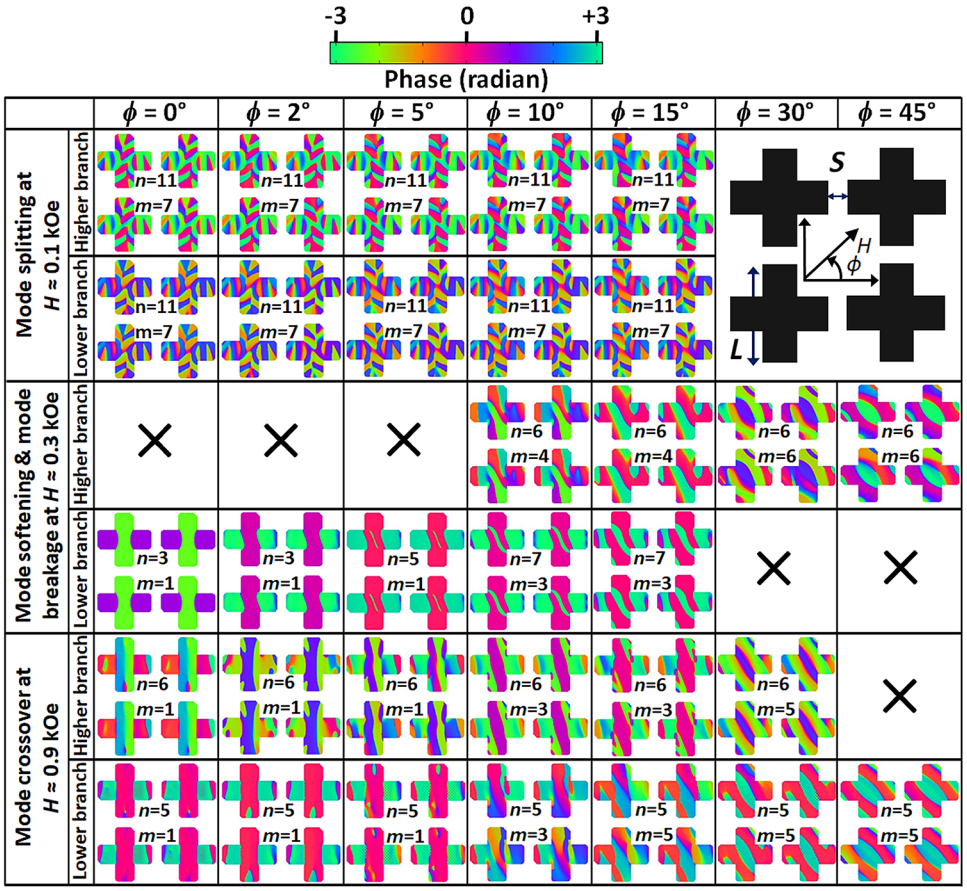

FIG. 5. Simulated spatial distribution of phase profiles corresponding to different salient SW modes at seven ϕ values and three different bias-field values for a $Ni_{80}Fe_{20}$ nanocross array with $L = 600$ nm. The color map is shown at the top of the figure.

the SEM images and a 2D periodic boundary condition (2D PBC) was applied for considering large areas of the arrays studied experimentally. The arrays are discretized into a number of rectangular prism-like cells of $4 \times 4 \times 20$ nm^3 dimensions. The material parameters of the sample such as γ, M_s, and H_K used in the simulations are extracted from the Kittel fit of the bias-field-dependent frequency of the Py thin film as discussed earlier, while the exchange stiffness constant $(A_{ex}) = 1.3 \times 10^{-6}$ erg/cm is taken from literature [36]. The damping constant is used as $\alpha = 0.008$ during dynamic simulations. The detailed methods of simulations are described elsewhere. Figures 2–4 show the simulated SW frequencies as a function of the magnetic field (unfilled symbols), which reproduce all the important features of the experimental results very well. We further simulate the power and phase profiles of the SW modes using a home-built code [37]. Figure 5 shows the simulated spatial distribution of phase profiles for various SW modes of the nanocross array with $L = 600$ nm at three different bias fields (H) and seven different ϕ values. The power profiles of the same are shown in Fig. S1 [38]. SW modes with an azimuthal character [32] do not show significant changes with ϕ due to azimuthal symmetry. The simulated spatial distribution of phase and power profiles corresponding to the two highest frequency branches, which merge with the reduction of H and an intermediate frequency branch at $H = 0.9$ kOe for the nanocross array with $L = 600$ nm are shown in Figs. S2 and S3, respectively

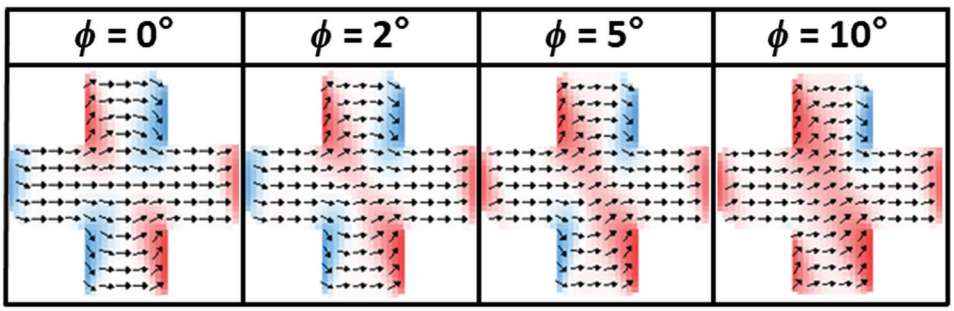

FIG. 6. Simulated static magnetic configurations for a nanocross array with arm length (L) of 600 nm at bias field $(H) = 0.5$ kOe for four different ϕ values. We have shown a single cross from the center of the array to prominently represent spin configurations.

[38]. The new mode, which appears from the splitting of the highest frequency branch at a higher H value, and the intermediate frequency branch, which shows a monotonic increase of the resonance frequency with H, both show an azimuthal character instead of a Damon-Eshbach (DE) character. We mainly focus here on radial SW modes. As ϕ changes, the phase profiles of both of the SW modes of feature (a) remain the same. These modes show a mixed backward volume (BV; n) and Damon-Eshbach (DE; m)-like character with mode quantization numbers $n = 11$ and $m = 7$ with opposite phases. The higher frequency branch of feature (a) disappears at $\phi \approx 15°$ for $L = 600$ nm. From the phase profile, the reason for the disappearance of mode softening with the increase of ϕ becomes clear. Mode softening is the result of the sudden switching of the magnetic configuration from the S state to the onion state. Figure 6 shows that a subtle increase in ϕ wipes away the onion state and the S state appears and stabilizes with further increase in ϕ as the bias field helps to align the spins accordingly. Consequently, as ϕ increases, the height of the minima due to mode softening decreases and the position of the minima shifts to a higher field value. For $H \approx 0.3$ kOe at $\phi \geq 5°$, the S state of magnetic configuration starts to arise again. Beyond the critical angle (ϕ_a), a mode crossover appears at the position of the minima, which is probably due to the reformation of the S state. For feature (b) at $\phi = 0°$, the mode quantization numbers are $n = 3$ and $m = 1$, which transform to a new mode with $n = 7$ and $m = 3$ at $\phi = 15°$ for $H = 0.3$ kOe. A new SW mode appears at the position of mode softening due to mode splitting at $\phi \approx 10°$ with mode quantization numbers $n = 6$ and $m = 4$ for $\phi = 10°$, which changes to $n = 6$ and $m = 6$ for $\phi = 45°$. The higher frequency branch of feature (c) changes qualitatively with the variation of ϕ. The mode quantization numbers of this mode are modified to $n = 6$ and $m = 5$ at $\phi = 30°$ from $n = 6$ and $m = 1$ at $\phi = 0°$. The mode quantization numbers of the lower frequency branch of feature (b) are $n = 5$ and $m = 1$ at $\phi = 0°$, which transform to $n = 5$ and $m = 5$ at $\phi = 45°$. The size of the nanocross structure also has a significant effect on the above-mentioned features (Table I). For feature (a), the ϕ_a value at which the disappearance of mode softening and the creation of a new mode crossover occur decreases with the reduction in L. This confirms that the bias field is more crucial for the lower dimension of nanocross in the case of mode softening. The ϕ_a value related to the disappearance of mode splitting at the lower field decreases monotonically with the decrement in L. The competition between the spin configurations in the two orthogonal arms is the reason for the appearance of this mode splitting. As L decreases, the competition gets weaker as configurational anisotropy drops, which might be a possible reason for the decrease of ϕ_b with a reduction in L. Interestingly, the ϕ_c values in feature (c) increase with the increment in L. The higher frequency branch between the two modes of this mode crossover is primarily showing a BV-like mode character and it appears at $H \approx 0.7$ kOe for $L = 600$ nm. This mode crossover shifts to a higher H value as L decreases. This is responsible for the increment of ϕ_c with the decrease of L. At $\phi = 45°$, the components of the bias field in both the orthogonal arms become equal, which may be responsible for the occurrence of the minima in the lowest frequency mode at an intermediate H value. A new mode splitting appears at a higher H value for $\phi = 45°$, which is independent of the size of the nanocross in this size regime.

To further understand the dynamics, we have numerically calculated the magnetostatic field distributions in the nanocross arrays and the corresponding contour plots are shown in Fig. 7(a) for four different orientations (ϕ) of

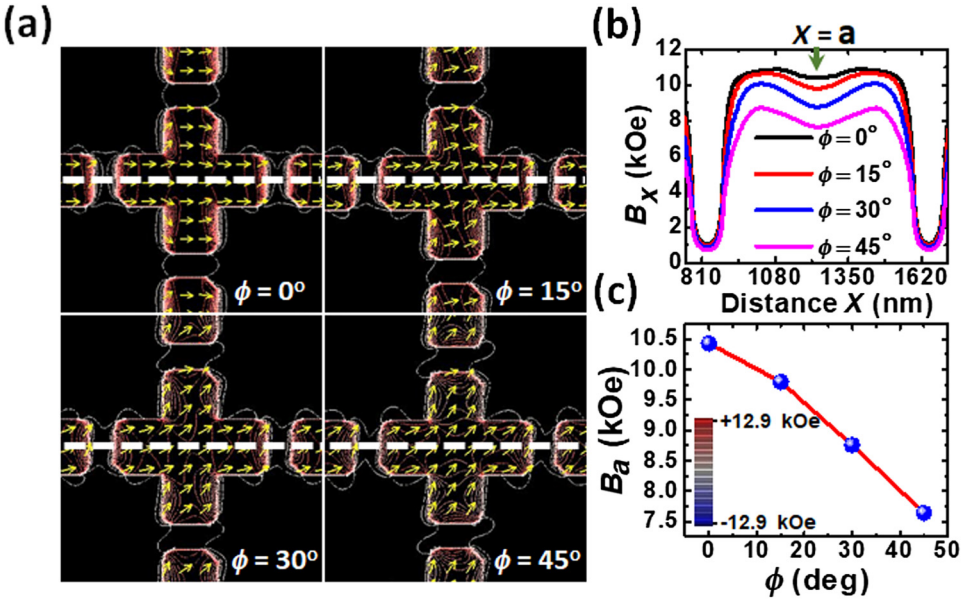

FIG. 7. (a) Contour plots of the simulated magnetostatic field distribution in a $Ni_{80}Fe_{20}$ nanocross array with arm length $L = 600$ nm in four different orientations (ϕ) of the bias field at $H = 0.6$ kOe. Line scans are taken along the white dotted lines. (b) Line scans of the simulated magnetostatic fields. The color map is shown in the inset of the bottom right of the figure. (c) Effective magnetic field at the center of the nanocross for different ϕ values.

the bias field. The important observation here is that with the increase of the ϕ value, the magnetic stray field-line density inside the nanocross structures increases, which is probably due to increase of the uncompensated magnetic charges in the nanocross structures in the direction of the bias field along both arms. Line scans of the fields along the dashed lines are presented in Fig. 7(b), which reveal an important feature. With the increase of ϕ, the internal fields decrease monotonically as plotted in Fig. 7(c). For $\phi = 0°$, the maximum stray field value is $B_x \approx 10.4$ kOe, which decreases to $B_x \approx 7.6$ kOe at $\phi = 45°$. In particular, a reduction of the internal field is observed near the center of the cross with an increase in ϕ. This feature is probably responsible for the increase of ϕ_c with a reduction in L. Figure 7(b) shows that the width of the stray field distribution along the x axis at maximum B_x value decreases with an increase in ϕ. The calculated magnetostatic field distributions indicate weak intercross stray magnetic fields. However, even such a weak interaction field has some effect on the dynamics, particularly at the lower bias-field value. We perform FMR measurement for nanocross arrays with an arm length (L) of 600 nm and with edge-to-edge separations (S) of 150, 250, and 350 nm. Figure S4 [38] shows that the variation of S from 150 to 250 nm affects the minimum in the frequency for the lowest frequency branch due to mode softening, while no further changes occur as S is increased to 350 nm.

Figure 8 provides an exemplary demonstration of how the SW propagation direction can be manipulated using a nanocross array. To that end, using OOMMF software, we launch a time-varying field of "sinc" profile (frequency cutoff of 30 GHz) at the center of the array over a small square region of 100 $\times$ 100 nm^2 area. We then simulate the propagation of the SW mode at $f = 8.4$ GHz for different orientations of the bias field. For $\phi = 0°$, the beam propagates along the vertical direction, for $\phi = 90°$, the beam propagates along the horizontal direction, for $\phi = 25°$, the beam propagates nearly isotropically in all directions, while at $\phi = 45°$, the beam ceases to propagate. This property may lead to possible applications of the nanocross array as a directional coupler or splitter. Figure S5 [38] demonstrates a proposal of how a densely packed nanocross array may be used as a frequency-dependent coupler. We perform further micromagnetic simulations to demonstrate possible applications of nanocross arrays as magnetic storage bits as shown in Fig. S6 [38]. The above possible applications promote ferromagnetic nanocross arrays as building blocks of a variety of spintronic and magnonic devices.

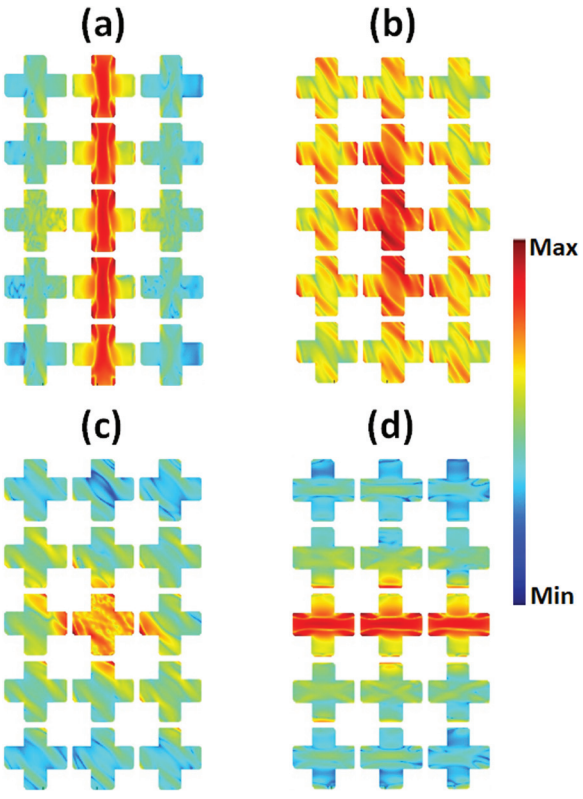

FIG. 8. Simulated power profiles of spin-wave modes of frequency (f) 8.4 GHz excited locally at the center of the array for (a) $\phi = 0°$, (b) $\phi = 25°$, (c) $\phi = 45°$, and (d) $\phi = 90°$ geometries.

IV. CONCLUSIONS

In summary, we investigate the magnetization dynamics in $Ni_{80}Fe_{20}$ nanocross arrays of varying sizes as a function of the orientation (ϕ) of an external bias magnetic field using a broadband FMR technique. As the bias field orientation (ϕ) deviates from 0°, the chances of formation of the onion state decrease. Consequently, the height of the dip in the lowest frequency branch reduces and the dip position shifts to a higher H value. Further increase of ϕ causes a new mode crossover at the lower H value in the place of the dip. Interestingly, the frequency difference between modes for mode crossover at a higher H value increases with the increment of ϕ and further increases of ϕ leads toward the disappearance of this high-field crossover resulting in two nearly parallel SW modes at $\phi = 30°$, while at $\phi = 45°$, the higher frequency branch disappears. The intermediate frequency branch shows a monotonic increase of frequency with the bias field. The orientation of the bias magnetic field (ϕ) strongly affects the Y-shaped mode splitting of the highest frequency branch at a lower H. The frequency gap between these two modes decreases with the increment of ϕ. Finally, at $\phi = \phi_b$, this mode splitting disappears. Higher field mode splitting shifts to a lower H value with the enhancement of ϕ and finally disappears. The number of SW modes decreases at $\phi = 45°$ compared to $\phi = 30°$. At $\phi = 45°$, the lowest frequency branch again shows a minimum at the intermediate H. A simulated SW modes profile shows that the modes showing strong dependence on the bias-field angle are of mixed

BV & DE character. Interestingly, the DE mode quantization number m increases with ϕ for most SW modes. With the variation of the nanocross dimension, both quantitative and qualitative variations of the magnetization dynamics occur. Calculated magnetostatic field distributions reveal the origin of the variation in the SW mode frequencies and mode profiles. Such an ability to tune the spin configuration and magnetization dynamics in a nanocross structure by a subtle variation of the external bias-field angle is very important for the design of magnetic storage, memory, logic, and magnonic devices as demonstrated by our further micromagnetic simulations.

ACKNOWLEDGMENTS

The authors gratefully acknowledge the financial support from the Department of Science and Technology, Government of India under Grant No. SR/NM/NS-09/2011(G) and S. N. Bose National Centre for Basic Sciences, India (Grant No. SNB/AB/18-19/211).

[1] S. D. Bader, Opportunities in nanomagnetism, Rev. Mod. Phys. **78**, 1 (2006).

[2] S. O. Demokritov, B. Hillebrands, and A. N. Slavin, Brillouin light scattering studies of confined spin waves: Linear and nonlinear confinement, Phys. Rep. **348**, 441 (2001).

[3] J. I. Martin, J. Nogues, K. Liu, J. L. Vicent, and Ivan K. Schuller, Ordered magnetic nanostructures: Fabrication and properties, J. Magn. Magn. Mater. **256**, 449 (2003).

[4] B. D. Terris and T. Thomson, Nanofabricated and self-assembled magnetic structures as data storage media, J. Phys. D: Appl. Phys. **38**, R199 (2005).

[5] T. Thomson, G. Hu, and B. D. Terris, Intrinsic Distribution of Magnetic Anisotropy in Thin Films Probed by Patterned Nanostructures, Phys. Rev. Lett. **96**, 257204 (2006).

[6] Y. Wang, F. Xiu, Y. Wang, J. Zou, W. P. Beyermann, Y. Zhou, and K. L. Wang, Coherent magnetic semiconductor nanodot arrays, Nanoscale Res. Lett. **6**, 134 (2011).

[7] A. Imre, G. Csaba, L. Ji, A. Orlov, G. H. Bernstein, and W. Porod, Majority logic gate for magnetic quantum-dot cellular automata, Science **311**, 205 (2006).

[8] S. Kaka, M. R. Pufall, W. H. Rippard, T. J. Silva, S. E. Russek, and J. A. Katine, Mutual phase-locking of microwave spin torque nano-oscillators, Nature **437**, 389 (2005).

[9] J. M. Shaw and T. J. Silva, Spin dynamics and mode structure in nanomagnet arrays: Effects of size and thickness on line width and damping, Phys. Rev. B **79**, 184404 (2009).

[10] P. P. Horley, A. Sukhov, J. Berakdar, and L. G. Trapaga-Martinez, Influence of dipole-dipole interactions on the angular dependence of ferromagnetic resonance spectra in arrays of Fe/FexOy core/shell nanocubes, Eur. Phys. J. B **88**, 165 (2015).

[11] V. Novosad, K. Yu. Guslienko, H. Shima, Y. Otani, S. G. Kim, K. Fukamichi, N. Kikuchi, O. Kitakami, and Y. Shimada, Effect of interdot magnetostatic interaction on magnetization reversal in circular dot arrays, Phys. Rev. B **65**, 060402 (2002).

[12] A. Barman, S. Wang, J. D. Maas, A. R. Hawkins, S. Kwon, A. Liddle, J. Bokor, and H. Schmidt, Magneto-optical observation of picosecond dynamics of single nanomagnets, Nano Lett. **6**, 2939 (2006).

[13] P. S. Keatley, P. Gangmei, M. Dvornik, R. J. Hicken, J. R. Childress, and J. A. Katine, Large amplitude magnetization dynamics and the suppression of edge modes in a single nanomagnet, Appl. Phys. Lett. **98**, 082506 (2011).

[14] G. Gubbiotti, G. Carlotti, T. Okuno, M. Grimsditch, L. Giovannini, F. Montoncello, and F. Nizzoli, Spin dynamics in thin nanometric elliptical Permalloy dots: A Brillouin light scattering investigation as a function of dot eccentricity, Phys. Rev. B **72**, 184419 (2005).

[15] G. Gubbiotti, M. Conti, G. Carlotti, P. Candeloro, E. D. Fabrizio, K. Y. Guslienko, A. Andre, C. Bayer, and A. N. Slavin, Magnetic field dependence of quantized and localized spin wave modes in thin rectangular magnetic dots, J. Phys.: Condens. Matter **16**, 7709 (2004).

[16] C. Schoeppner, K. Wagner, S. Stienen, R. Meckenstock, M. Farle, R. Narkowicz, D. Suter, and J. Lindner, Angular dependent ferromagnetic resonance analysis in a single micron sized cobalt stripe, J. Appl. Phys. **116**, 033913 (2014).

[17] X. Cui, S. Yakata, and T. Kimura, Directional dependence of vortex core resonance in a square-shaped ferromagnetic dot, Physica E **75**, 28 (2016).

[18] Y. P. Ivanov, A. I. Ilin, E. V. Pustovalov, K. V. Nefedov, and L. A. Chebotkevich, Effect of the shape anisotropy and configurational anisotropy on the magnetic structure of ferromagnetic naodots, Phys. Metals Metallogr. **113**, 222 (2012).

[19] B. K. Mahato, B. Rana, D. Kumar, S. Barman, S. Sugimoto, Y. Otani, and A. Barman, Tunable spin wave dynamics in two-dimensional $Ni_{80}Fe_{20}$ nanodot lattices by varying dot shape, Appl. Phys. Lett. **105**, 012406 (2014).

[20] Z. Liu and R. D. Sydora, Shape effects on magnetization state transitions in individual 160-nm diameter Permalloy disks, Phys. Rev. B **77**, 174410 (2008).

[21] V. V. Kruglyak, P. S. Keatley, A. Neudert, R. J. Hicken, J. R. Childress, and J. A. Katine, Imaging Collective Magnonic Modes in 2D Arrays of Magnetic Nanoelements, Phys. Rev. Lett. **104**, 027201 (2010).

[22] V. V. Kruglyak, A. Barman, and R. J. Hicken, Picosecond magnetization dynamics in nanomagnets: Crossover to nonuniform precession, Phys. Rev. B **71**, 220409 (2005).

[23] S. Jung, B. Watkins, L. Delong, J. B. Ketterson, and V. Chandrasekhar, Ferromagnetic resonance in periodic particle arrays, Phys. Rev. B **66**, 132401 (2002).

[24] G. N. Kakazei, Yu. G. Pogorelov, M. D. Costa, T. Mewes, P. E. Wigen, P. C. Hammel, V. O. Golub, T. Okuno, and V. Novosad, Origin of fourfold anisotropy in square lattices of circular ferromagnetic dots, Phys. Rev. B **74**, 060406 (2006).

[25] O. N. Martyanov, V. F. Yudanov, R. N. Lee, S. A. Nepijko, H. J. Elmers, C. M. Schneider, and G. Schonhense, Ferromagnetic resonance investigation of collective phenomena in two-dimensional periodic arrays of Co particles, Appl. Phys. A **81**, 679 (2005).

[26] Z. K. Wang, H. S. Lim, V. L. Zhang, J. L. Goh, S. C. Ng, H. L. Su, S. L. Tang, and M. H. Kuok, Collective spin waves in high-density two-dimensional arrays of FeCo nanowires, Nano Lett. **6**, 1083 (2006).

[27] G. Gubbiotti, M. Madami, S. Tacchi, G. Carlotti, and T. Okuno, Normal mode splitting in interacting arrays of cylindrical permalloy dots, J. Appl. Phys. **99**, 08C701 (2006).

[28] A. Barman and S. Barman, Dynamic dephasing of magnetization precession in arrays of thin magnetic elements, Phys. Rev. B **79**, 144415 (2009).

[29] K. Machida, T. Tezuka, T. Yamamoto, T. Ishibashi, Y. Morishita, A. Koukitu, and K. Sato, Magnetic structure of cross-shaped permalloy arrays embedded in silicon wafers, J. Magn. Magn. Mater. **290**, 779 (2005).

[30] B. K. Mahato, B. Rana, R. Mandal, D. Kumar, D. Kumar, S. Barman, Y. Fukuma, Y. Otani, and A. Barman, Configurational anisotropic spin waves in cross-shaped $Ni_{80}Fe_{20}$ nanoelements, Appl. Phys. Lett. **102**, 192402 (2013).

[31] K. Nanayakkara, A. P. Jacob, and A. Kozhanov, Spin wave scattering and interference in ferromagnetic cross, J. Appl. Phys. **118**, 163904 (2015).

[32] K. Adhikari, S. Choudhury, R. Mandal, S. Barman, Y. Otani, and A. Barman, Bias field tunable magnetic configuration and magnetization dynamics in $Ni_{80}Fe_{20}$ nano-cross structures with varying arm length, J. Appl. Phys. **121**, 043909 (2017).

[33] A. Barman and J. Sinha, *Spin Dynamics and Damping in Ferromagnetic Thin Films and Nanostructures* (Springer International Publishing AG, Switzerland, 2018).

[34] Charles Kittel, On the theory of ferromagnetic resonance absorption, Phys. Rev. **73**, 155 (1948).

[35] M. Donahue and D. G. Porter, OOMMF User's Guide, Version 1.0, NIST Interagency Report No. 6376, National Institute of Standard and Technology, Gaithersburg, MD, 1999.

[36] K. H. J. Buschow, *Handbook of Magnetic Materials* (North Holland, Amsterdam, The Netherlands, 2009).

[37] D. Kumar, O. Dmytriiev, S. Ponraj, and A. Barman, Numerical calculation of spin wave dispersions in magnetic nanostructures, J. Phys. D: Appl. Phys. **45**, 015001 (2012).

[38] "See Supplemental Material at http://link.aps.org/supplemental/10.1103/PhysRevApplied.10.044010 for (a) simulated spatial distribution of phase and power profiles corresponding to different SW modes, (b) experimental surface plots of bias-field-dependent SW mode frequencies for nano-cross arrays with varying edge-to-edge separation, (c) simulated power profile of SW modes of different frequencies for densely packed nano-cross array, (d) simulated static magnetic configurations for nano-cross array after applying different magnitudes of spin-polarized current".